Bioresource Technology 280 (2019) 313–324

Contents lists available at ScienceDirect

Bioresource Technology

journal homepage: www.elsevier.com/locate/biortech

Kinetics, thermodynamics, gas evolution and empirical optimization of (co-) combustion performances of spent mushroom substrate and textile dyeing sludge

Jianli Huang[a], Jingyong Liu[a,*], Jiahong Kuo[a], Wuming Xie[a], Xiaochun Zhang[a], Kenlin Chang[a,b], Musa Buyukada[c], Fatih Evrendilek[d,e]

[a] *Guangzhou Key Laboratory Environmental Catalysis and Pollution Control, Guangdong Key Laboratory of Environmental Catalysis and Health Risk Control, School of Environmental Science and Engineering, Institute of Environmental Health and Pollution Control, Guangdong University of Technology, Guangzhou 510006, China*

[b] *Institute of Environmental Engineering, National Sun Yat-Sen University, Kaohsiung 80424, Taiwan*

[c] *Department of Chemical Engineering, Bolu Abant Izzet Baysal University, Bolu 14052, Turkey*

[d] *Department of Environmental Engineering, Bolu Abant Izzet Baysal University, Bolu 14052, Turkey*

[e] *Department of Environmental Engineering, Ardahan University, Ardahan 75002, Turkey*

ARTICLE INFO

Keywords:
Textile dyeing sludge
Spent mushroom substrate
Co-combustion
Kinetic analysis
TG-MS

ABSTRACT

Spent mushroom substrate (SMS) and textile dyeing sludge (TDS) were (co-)combusted in changing heating rates, blend ratios and temperature. The increased blend ratio improved the ignition, burnout and comprehensive combustion indices. A comparison of theoretical and experimental thermogravimetric curves pointed to significant interactions between 350 and 600 °C. High content of Fe_2O_3 in TDS ash may act as catalysis at a high temperature. Ignition activation energy was lower for TDS than SMS due to its low thermal stability. 40% SMS appeared to be the optimal blend ratio that significantly decreased the activation energy, as was verified by the response surface methodology. D3 model best described the (co-)combustions. SMS led to more NO and NO_2 emissions at about 300 °C and less HCN emission than did TDS. The addition of 40% SMS to TDS lowered SO_2 emission. The co-combustion of TDS and SMS appeared to enhance energy generation and emission reduction.

1. Introduction

The growing quantity of hazardous wastes has been posing an increasingly significant threat to the environmental and human health (Dong et al., 2017). One such waste is textile dyeing sludge (TDS), the by-product of the wastewater treatment process, since it contains toxic organic chemicals, recalcitrant compounds, and heavy metals (Liu et al., 2018a). Currently, the annual generation rate of TDS is about 21 million tons in China and is still rising from the rapid population and consumption growth (Xie et al., 2018b). The traditional TDS disposal methods of landfilling and composting are no longer considered socially, economically and environmentally benign due to their high costs and risks. With the implementation of increasingly strict environmental laws, the incineration of sludge is being regarded as the most efficient disposal method (Peng et al., 2015). The advanced combustion technologies make the waste stream of TDS a promising solid feedstock with the multiple objectives of flame stabilization, waste reduction, energy generation, and emission reduction (Peng et al., 2015). Coal-fired power plants of many European countries have adopted the co-combustion of solid wastes including TDS as the most appropriate disposal method (Liu et al., 2018a; Xie et al., 2018b).

Since the high ash content and low calorific value of TDS limit its application in a mono-combustion (Peng et al., 2015; Xie et al., 2018a), it is essential to find an auxiliary biofuel to improve its combustion performance. The co-combustion of coal and biomass can reduce the mobility of Pb, Cd, and Zn to improve ash deposition quality (Guo and Zhong, 2018a). The co-combustion performances of TDS and oily, sewage or paper mill sludge were explored with various biofuels such as pomelo peel, microalgae, and wood (Deng et al., 2016; Peng et al., 2015; Xie et al., 2018b). These studies indicated that the selection of a suitable blend ratio improved the co-combustion performances. However, co-combustion with coal does not appear to be favorable due to the limited coal reserves, and associated greenhouse gas emissions. The utilization of biomass and biowaste for energy generation has attracted wide attention owing to their renewable and carbon-neutral characteristics (Ma et al., 2017).

---

[*] Corresponding author.
E-mail address: Liujy@gdut.edu.cn (J. Liu).

https://doi.org/10.1016/j.biortech.2019.02.011
Received 19 December 2018; Received in revised form 31 January 2019; Accepted 1 February 2019

The Chinese sectors of mushroom cultivation and processing are annually generating over 13 million tons of spent mushroom substrate (SMS) that has exceeded its disposal rate via agricultural applications (Huang et al., 2018). This case has in turn intensified the search for its environmentally and economically effective disposal since SMS has favorable combustion properties such as high volatiles and low ashes as an alternative biofuel. A better understanding, designing, and managing of the co-combustion systems and their application performances on the industrial-scale require the quantification of their kinetics, thermodynamics and optimal operational settings (Cai et al., 2018; Gil et al., 2010). Thermogravimetric (TG) analysis and its derivative (DTG) curves provide a real-time dynamic monitoring of mass loss and decomposition rate from which both kinetic and thermodynamic parameters are derived. Apparent activation energy (E_a) is one such essential kinetic parameter estimated as a function of a given conversion degree (α). From E_a values, thermodynamic parameters such as the pre-exponential factor (A), and changes in Gibbs free energy (ΔG), entropy (ΔS) and enthalpy (ΔH) are further estimated.

To optimize the operational conditions (e.g., temperature, heating rate, blend ratio), the systematically changing experimental designs are essential (Joshi et al., 2018). For example, the optimal combustion variables, and their uncertainties and sensitivities were determined using Box–Behnken design (BBD), a subset of response surface methodology (RSM) (Buyukada, 2017a; Lin et al., 2018). BBD has been successfully applied to maximize predictability and to minimize experimental runs and errors associated with the multiple and non-linear responses as the typical co-combustion behaviors (Buyukada, 2017a; Joshi et al., 2018).

The gaseous products as monitored via TG-mass spectroscopy (TG-MS) analysis are also significant to determine the economic and environmental efficiency of the co-combustion process. The emissions of the air pollutants (e.g., CO_2, NO_x, SO_x, NH_3, and HCN) differ according to the various thermal degradation stages, and the major components of the fuels. However, there exists no study about if and how the co-combustion of TDS and SMS can serve to alleviate the challenges of improving energy generation and efficiency as well as environmental quality and sustainability through decentralized combustion technologies (Wang et al., 2016).

In light of the above gaps and opportunities, the objectives of this study were to (1) characterize the (co-)combustions of TDS and SMS using (TG)-MS analyses, (2) evaluate the co-combustion performances using the ignition, burnout and comprehensive combustion indices as well as kinetic and thermodynamic analysis and (3) optimize the operational conditions using BBD.

2. Materials and methods

2.1. Sample preparation

TDS samples were collected from a wastewater treatment plant of a textile dyeing factory in Foshan of the Guangdong province of China. Textile wastewater was dewatered using a plate-frame pressure filtration to obtain solid TDS samples. SMS samples were gathered from a mushroom cultivation factory in Xiamen of the Fujian province of China. The TDS and SMS samples were naturally sun-dried to remove their moisture, pulverized to smaller particles and passed through a sieve with a 74-µm pore size. For a better understanding of the fuel properties, ultimate and proximate analyses in an air-dried basis were conducted and shown in Table 1. Finally, these samples were dried in an oven at 105 °C for 24 h prior to being put into a desiccator for further analyses. In the experiments, the six blend ratios of TDS to SMS were prepared and coded thus: TDS, 90TDS/10SMS, 80TDS/20SMS, 70TDS/30SMS, 60TDS/40SMS, and SMS. To compare TDS and SMS, their major ash components analyses were conducted using various methods (Table 1). Al and Na were determined using the chemical titration method and an atomic absorption spectrophotometer (AAS-240, USA), respectively. The other components were determined using an inductively coupled plasma optical emission spectrometer (ICP-OES, ICAP7400).

Table 1
The main fuel characteristic of TDS and SMS on an air-dried basis.

Analyses	TDS	SMS	Composition (wt %)	TDS	SMS
Ultimate analyses (wt %)			CaO	5.58	1.81
C	16.62	42.49	SiO_2	4.33	1.62
H	3.02	5.80	K_2O	0.18	1.50
N	3.33	2.15	MgO	0.84	1.38
S	6.82	0.10	Al_2O_3	0.47	0.32
Proximate analyses (wt %)			Fe_2O_3	35.80	0.16
Moisture content	5.70	8.89	MnO	0.15	0.02
Ash	62.85	10.90	Na_2O	3.84	0.01
Volatiles content	27.83	62.93	P_2O_5	1.43	3.53
Fixed carbon	3.62	17.28	Cl^-	0.34	0.15

2.2. TG analysis

The three heating rates of 10, 20, and 30 °C/min were used in TG analysis until a final temperature of 1000 °C was reached using a TG analyzer (STA 409 NETZSCH). About 6 mg of the samples were placed into an alumina crucible and then heated at a constant rate from room to final temperature at a stable air gas flow rate of 50 mL/min. Prior to the experiments, a blank experiment was conducted to obtain a baseline to reduce the systematic errors. Also, a random sampling was conducted in triplicates to ensure the reproducibility and that the resultant errors were within ± 2%.

The (D)TG data can be used to estimate the relative combustion parameters to evaluate the combustion performance. The three common parameters used in related literature include ignition index (D_i), burnout index (D_b), and comprehensive combustion index (CCI). D_i and D_b were determined as follows (Li et al., 2011):

$$D_i = \frac{(-R_P)}{t_i \times t_p} \tag{1}$$

$$D_b = \frac{(-R_P)}{\Delta t_{1/2} \times t_p \times t_b} \tag{2}$$

where $-R_p$ is maximum mass loss rate; and t_p, t_i, t_b and $\Delta t_{1/2}$ refer to peak temperature (T_p), ignition temperature (T_i), burnout temperature (T_b), and the temperature range of half peak width of $-R_p$ ($\Delta T_{1/2}$), respectively. TG and DTG tangent method can be used to define T_i according to Li et al. (2011). T_b is the temperature when 98% of weight loss is completed during the entire combustion process. CCI can be expressed using Eq. (3) (Chen et al., 2017b):

$$CCI = \frac{(-R_P) \times (-R_V)}{T_i^2 \times T_b} \tag{3}$$

where $-R_V$ is average mass loss rate. A high CCI indicates a better combustion property and faster burnout for the samples.

2.3. TG-MS experiments

The gaseous products were monitored using TG-MS (Rigaku Thermo Mass Photo, Japan). About 4 mg of the samples were put into an alumina crucible in the TG furnace and then were heated from room temperature to 1000 °C at a heating rate of 10 °C/min. To avoid a possible confusion in determining N_2 and CO ($m/z = 28$) products in the air atmosphere (79% N_2/21% O_2), 79% He and 21% O_2 were mixed to be used as the oxidation atmosphere. The major gas products during the combustion process in the m/z range of 1 to 150 were identified using a quadrupole detector for the mass separation. The electron ionization voltage was set at 70 eV.

2.4. Kinetic and thermodynamic analyses

The co-combustion involves a complex thermochemical reaction due to the complex compositions of the multiple solid fuels. The co-combustion systems and their optimal conditions can be better understood using kinetic and thermodynamic analyses (Gil et al., 2010).

The decomposition rate can be expressed by Eq. (4):

$$\frac{d\alpha}{dt} = k(T)\cdot f(\alpha) = A\exp\left(-\frac{E_a}{RT}\right)\cdot f(\alpha) \tag{4}$$

where α and R represent conversion degree, and universal gas constant (8.314 J/(mol·K)), respectively. $f(\alpha)$ is the reaction mechanism function for the decomposition stage of solid fuels. E_a is dependent on temperature and α. A constant heating rate (β) can be defined thus: $\beta = dT/dt$, hence Eq. (4) can be rewritten as follows:

$$\frac{d\alpha}{dT} = \frac{A}{\beta}\exp\left(-\frac{E_a}{RT}\right)\cdot f(\alpha) \tag{5}$$

The iso-conversional methods, also known as model-free methods, avoid the errors of selecting an improper reaction mechanism function to estimate accurate and reliable E_a values. In this study, the Flynn–Wall–Ozawa (FWO) and Kissinger–Akahira–Sunose (KAS) methods were used to estimate E_a values as the degradation kinetics of the solid biofuels.

Adopting the Doyle' approximation for the temperature integration, the FWO method can be expressed as follows (Müsellim et al., 2018):

$$\lg\beta = \lg\left(\frac{AE_a}{Rg(\alpha)}\right) - 2.315 - 0.4567\frac{E_a}{RT} \tag{6}$$

When $\lg\left(\frac{AE_a}{Rg(\alpha)}\right)$ was assumed to be a constant, a least square regression line was fitted in the relationship between $\lg\beta$ and $\frac{1}{T}$ based on the TG data with the three heating rates. The slope of the regression line was used to estimate E_a.

The KAS method can be described using Eq. (7) (Müsellim et al., 2018):

$$\ln\left(\frac{\beta}{T^2}\right) = \ln\left(\frac{AE_a}{Rf(\alpha)}\right) - \frac{E_a}{RT} \tag{7}$$

Similarly, for a certain α, the slope of a linear regression line of the plot of $\ln\left(\frac{\beta}{T^2}\right)$ and $\frac{1}{T}$ was used to estimate E_a. The four thermodynamic parameters of A, ΔG, ΔS and ΔH were further derived from E_a estimates as follows (Maia and Morais, 2016; Müsellim et al., 2018):

$$A = \left(\beta\cdot E_a\cdot\exp\left(\frac{E_a}{RT_p}\right)\right)/(RT_p^2) \tag{8}$$

$$\Delta H = E_a - RT \tag{9}$$

$$\Delta G = E_a + RT_p\ln\left(\frac{K_BT_p}{hA}\right) \tag{10}$$

$$\Delta S = (\Delta H - \Delta G)/T_p \tag{11}$$

where K_B and h represent the Boltzmann (1.381×10^{-23} J/K) and Plank (6.626×10^{-34} J·s) constants, respectively.

2.5. Reaction model selection

The Coats and Redfern method (CR) is the common method used in the thermal kinetic analysis of various feedstocks (Jiang et al., 2018). The CR method makes it possible to estimate the reaction mechanisms of the thermal oxidation process using TG data. The 17 common kinetic models of the solid-state reactions reported by Mallick et al (2018) were used in the kinetic analysis. Reaction function ($f(\alpha)$) and its integral form ($g(\alpha)$) depend mainly on the mathematical models of the reaction mechanisms. Using the CR method, Eq. (5) can be simplified as follows (Gil et al., 2010; Mallick et al., 2018):

$$\ln\frac{g(\alpha)}{T^2} = \ln\frac{AR}{\beta E} - \frac{E}{RT} \tag{12}$$

The reaction models were used to find out the best fitting mechanism for the different combustion stages. Once a suitable model was selected, the slope of the best-fit regression line of the plot of $\ln\frac{g(\alpha)}{T^2}$ versus $1/T$ was used to estimate E_a.

2.6. Box–Behnken design

The effects of blend ratio (%), heating rate (°C/min), and temperature (°C) on the two co-combustion responses of mass loss (ML, %) and mass loss rate (MLR, %/min) were quantified using BBD, a response surface methodology. A total of 17 experimental runs (including three replicates) for the three factors with three levels were performed, less than what a central composite design (CCD) required (Latchubugata et al., 2018). The three factors with the three levels were thus: heating rates (10, 20 and 30 °C/min), blend ratios (TDS, 80TDS/20SMS, and 60TDS/40SMS), and temperatures (200, 600 and 1000 °C). The Design Expert software was used to predict and optimize the responses of ML and MLR according to the operational parameters. The best-fit regression model was identified according to BBD with the highest adjusted (R^2_{adj}) and predictive (R^2_{pred}) coefficients of determination (Buyukada, 2017b).

3. Results and discussion

3.1. Comparative fuel properties

It is essential to understand the feedstock properties for a combustion reactor, as shown in Table 1. The higher volatiles contents of SMS than TDS indicated its more flammable substance and better combustion performance than TDS. The mono-combustion of a solid fuel with a high ash content such as TDS always poses the serious issues of slagging, agglomeration, and corrosion so as to decrease the combustion efficiency of a given boiler (Liu et al., 2018b). The large amounts of volatiles and fixed carbon of SMS may provide heat enough to maintain the TDS combustion. The higher N and S contents of TDS than SMS escalate the risk of more NO_x and SO_x emissions. Hence, their co-combustion may reduce the emissions. The composition analyses showed that TDS mainly contained Fe, Ca, Si, and Na, while SMS had P, Ca, Si, and K. The crystalline phases of the TDS and SMS ashes were determined using an X-Ray Diffraction (XRD, MiniFlex 600, Rigaku Corporation, Japan). The XRD patterns showed that Fe_2O_3 was the main mineral component of the TDS ash. As a flux agent, Fe_2O_3 decreased the ash fusion temperatures effectively, thus having a positive effect on the co-combustion (Shi et al., 2018). The combustion of the TDS ash may further induce the combustion of the other materials to improve the combustion performance owing to the catalytic effect of Fe_2O_3 (Wang et al., 2018b). Since P generally exists in the form of phosphate after the combustion, the P-rich ash of SMS renders the recovery of P possible, a new direction to be considered in the future studies.

3.2. Characterization of thermal degradation rate and amount

This study focused on the (co-)combustion properties of TDS and SMS at the heating rates of 10, 20 and 30 °C/min. Their (D)TG curves at 10 °C/min of the blends are located in between those of the individual solid fuels (Fig. 1). The significantly increased responses of mass loss and mass loss rate to the increased SMS fraction showed its more flammable substance and better combustion performance than TDS. Three and four peaks were observed in the DTG curves of TDS and SMS, respectively, due to the thermal degradations of their various components in the range of room temperature to 1000 °C (Fig. 1).

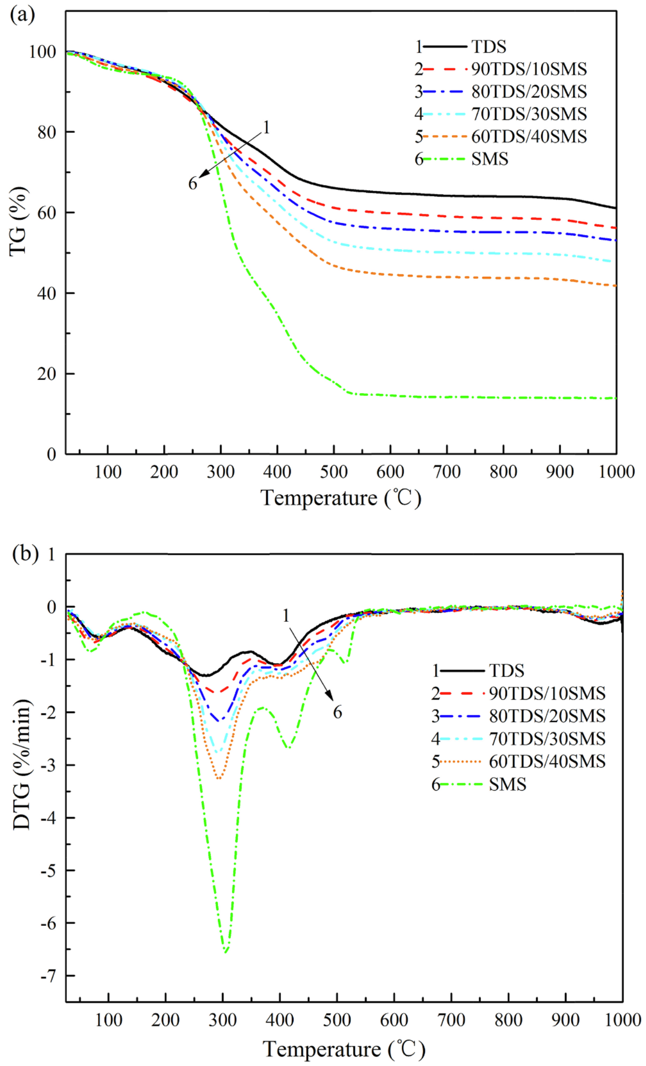

Fig. 1. (D)TG curves of TDS, SMS, and their blends at 10 °C /min.

Table 2

Estimates of combustion characteristic parameters and indices from TG data at 10°C/min as a function of SMS fraction of blends.

SMS fraction of blends	0%	10%	20%	30%	40%	100%
T_i (°C)	197.2	203.0	218.8	232.6	238.2	256.8
T_b (°C)	970.0	955.4	948.8	944.0	928.2	522.4
T_p (°C)	270.4	290.0	293.2	291.4	292.8	307.0
$\Delta T_{1/2}$ (°C)	259.8	230.6	189.2	94.8	89.6	70.0
$\Delta t_{1/2}$ (min)	25.44	22.70	18.73	9.41	8.90	6.89
$-R_v$ (%/min)	0.41	0.46	0.50	0.54	0.60	0.90
$-R_P$ (%/min)	1.31	1.64	2.16	2.77	3.26	6.68
CCI ($10^{-8}\%^2\text{min}^{-2}\text{°C}^{-3}$)	1.11	1.49	1.90	2.27	2.87	11.45
D_i ($10^{-3}\%/\text{min}^3$)	3.15	3.56	4.25	4.78	5.46	9.79
D_b ($10^{-4}\%/\text{min}^4$)	0.23	0.30	0.47	1.17	1.48	6.71
M_f (%)	62.21	56.18	53.10	47.81	41.86	13.85

$\Delta T_{1/2}$: temperature range between the half -R_P; -R_v: mean mass loss rate; and M_f: final residue at 1000 °C

The first peak at about 80 °C and the mass loss below 200 °C mainly resulted from the evaporation of moisture which was not further discussed in this study. At about 200 °C, the higher mass loss rate of TDS than SMS indicated the better decomposition behaviors of TDS at the low temperature, as was verified by the lower ignition temperature (T_i) of TDS (197.2 °C) than SMS (256.8 °C) (Table 2). Similarly, TDS was reported to contain the small-molecule organic compounds with weak chemical bonds that were easily biodegradable at a lower temperature (Peng et al., 2015). This finding supported the result that the volatiles matters of TDS were easily degraded at the lower temperature. SMS, a lignocellulosic material rich in (hemi)celluloses and lignin with a stable chemical structure, only began to degrade in the range of 220–550 °C.

The maximum mass loss rates ($-R_P$) of TDS and SMS were estimated at 1.31 and 6.68%/min at 270.4 and 307.0 °C, respectively. The decompositions of the small-molecule organic compounds of TDS, and (hemi)celluloses of SMS marked the main stages of mass losses. The mass loss of TDS between 350 and 600 °C may have resulted from the combustion of the macromolecule organic matter produced during the stabilization and biological treatment stages (Peng et al., 2015). The combustion of SMS was finished at 600 °C, while a small mass loss of TDS occurred between 900 and 1000 °C due to the decomposition of inorganic substances. The TDS ash mainly contained alkali (Na_2O), alkaline earth metals (e.g., CaO and MgO), Fe_2O_3, SiO_2, and richer heavy metals (e.g., Zn, Pb, Cu, Ni, and Cr). Pb, and Zn were reported to volatize at 940 °C, while $CaSO_4$ tended to degrade in the range of 800–1000 °C, but alkali and alkaline earth metals reacted with the trace elements at a higher temperature (Guo and Zhong, 2018a; Wang et al., 2008). This may account for the changes in the (D)TG curves of TDS and its blends at the high temperatures.

3.3. Comparative indices of co-combustion performances

A strong linear relationship was found between the blend ratio and the maximum mass loss rate ($-R_P$). The addition of SMS to TDS increased the $-R_P$, thermal reactivity and $-R_V$ values. The combustion of volatiles in turn generated more heat to accelerate the decomposition of incombustible materials. The contrasting effects on T_i and T_b were observed with the increased SMS (Table 2). The addition of SMS increased T_i and decreased T_b. The lack of a linear growth trend in T_i and T_b with the increased SMS may suggest a synergistic effect on the co-combustion. Their co-combustion improved the T_i and T_b properties of each other. The addition of more SMS changed the volatiles content, and thus, caused a less residual amount. Whether or not an interaction existed between SMS and TDS still remains to be explored in the next sections.

The significantly increased D_i, D_b and CCI with the increased SMS indicated its improvement of the TDS combustion. This result was supported by the other findings (Guo and Zhong, 2018b; Peng et al., 2015). According to Eq. (1), the main control over D_i by $-R_P$ in turn depended on the amount of volatiles matters. More heat releases with the higher SMS content improved the combustion properties of TDS. The lower CCI values of TDS ($1.11 \times 10^{-8}\%^2\,\text{min}^{-2}\,\text{°C}^{-3}$) than SMS ($11.45 \times 10^{-8}\%^2\,\text{min}^{-2}\,\text{°C}^{-3}$) at 10 °C/min pointed to the better combustion performance of SMS than TDS. The CCI value of SMS was higher than that of camellia seed shell ($8.15 \times 10^{-8}\%^2\,\text{min}^{-2}\,\text{°C}$) and rapeseed meal ($2.75 \times 10^{-8}\%^2\,\text{min}^{-2}\,\text{°C}$) (Chen et al., 2017b). An exponential relationship was found between CCI and blend ratio.

3.4. Interaction effects of blends

The interaction effect of the co-combustion means the involvement of the non-linear reaction mechanisms and not the simple sum of the additive effects of the individual biofuels. In the evaluation of the interactions, the experimental and theoretical TG and DTG curves were compared in Fig. 2. The theoretical curves were based on the following equation (Peng et al., 2015):

$$\text{(D)TG}_{\text{cal}} = \gamma_{\text{SMS}}\cdot\text{(D)TG}_{\text{SMS}} + \gamma_{\text{TDS}}\cdot\text{(D)TG}_{\text{TDS}} \qquad (13)$$

where γ_{SMS} and γ_{TDS} represent SMS and TDS fractions of the blends, while $\text{(D)TG}_{\text{SMS}}$ and $\text{(D)TG}_{\text{TDS}}$ are the experimental curves of SMS and TDS, respectively.

At below 350 °C, the similar rates of the experimental and theoretical mass loss pointed to no significant interaction during the stages of

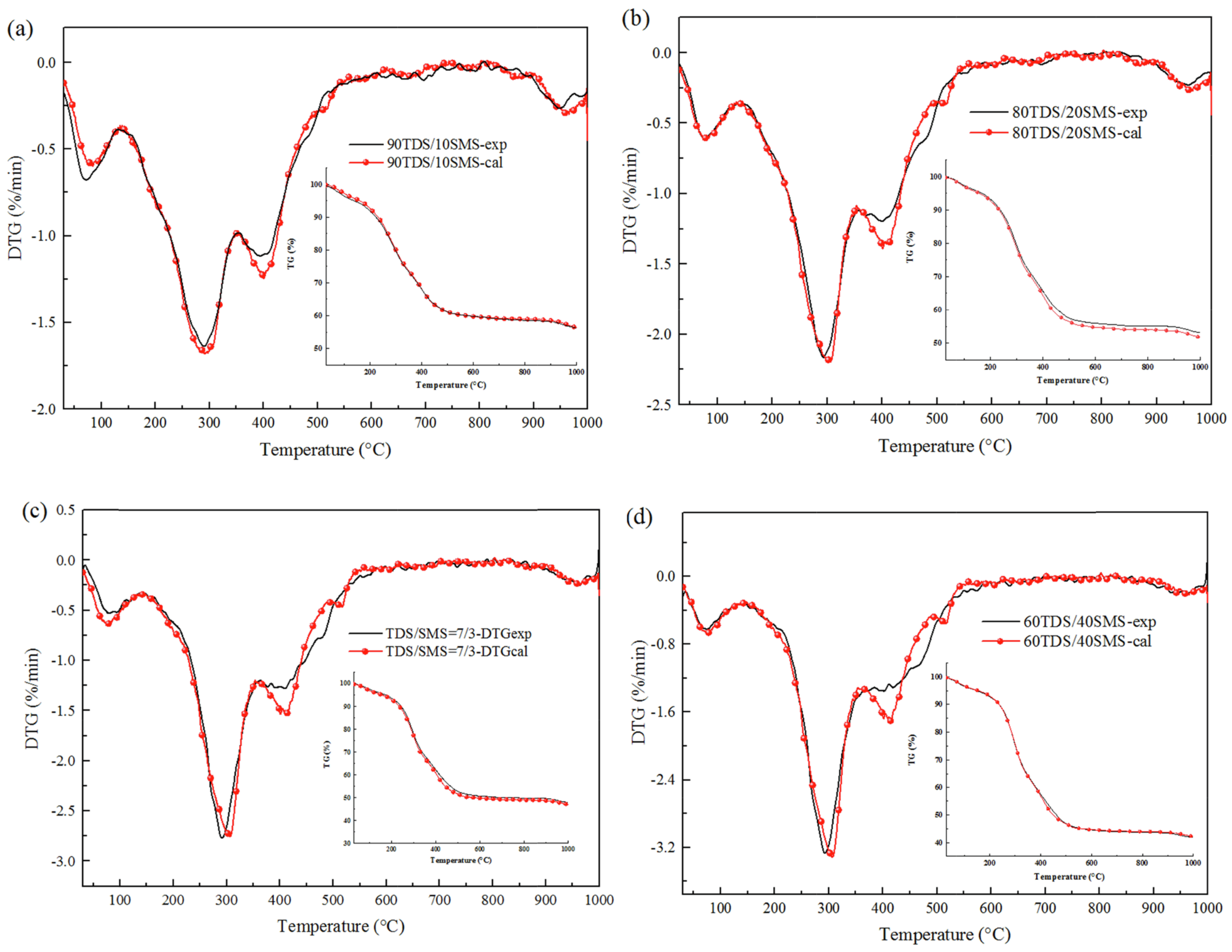

Fig. 2. A comparison of experimental versus theoretical TG-DTG curves with different SMS fractions.

water evaporation and volatiles combustion. In the range of 350–600 °C, the theoretical DTG curve of SMS exhibited a distinct weight loss peak, as with the experimental one. This suggested that some substances in TDS may hinder the combustion of fixed carbon in SMS and may promote the decomposition at a higher temperature. This case was supported by the interaction reported between 400 and 600 °C by Wang et al. (2011) that the partly absorbed heat from the SMS combustion adversely affected its combustion.

The mineral contents (e.g., Ca, K, and Mg) were found to produce a catalytic effect on the co-combustion of coke (Liu et al., 2013). The ash compositions of TDS and SMS (Table 1) showed that the minerals most probably acted as the catalyst. The catalytic effects can be weakened by the formation of the inactive alkali aluminosilicates, and the inactivated reactions between alkali metals and aluminosilicate minerals (Xie et al., 2018a). Hence, the interaction between TDS and SMS was more pronounced and complex in the co-combustion stage of fixed carbon.

The temperature of the maximum peak of mass loss (T_P) of the experimental curves was slightly lower than that of the theoretical curves due to the interaction between the fuels. The heat release from the combustion of volatiles matters appeared to accelerate the TDS decomposition and lowered the peak temperature. At 480 °C, the experimental DTG curve had a small shoulder peak, while the theoretical DTG curve exhibited a small peak at 520 °C. The decomposition peak moved to a lower temperature zone. This case may be attributed to the interaction between alkaline earth metals and metals of TDS and SMS so as to form a low melting point substance, thereby promoting the decomposition of the blends (Hu et al., 2015).

At 600 °C, the experimental and theoretical DTG curves were basically consistent, and the combustion was almost completed. The still unclear interaction mechanism of TDS and SMS may be explained in the following two possible ways (Deng et al., 2016; Guo and Zhong, 2018b). First, the heat release from the volatiles of SMS in the low temperature may promote the TDS decomposition. Second, biochar formed during the SMS decomposition can catalyze the TDS decomposition. Silicates, aluminates, and metal salts may also catalyze the decomposition of the two substances. However, the lower residues of the theoretical than experimental TG curves with some blends indicated that some blends may cause an incomplete combustion. This inhibition effect may be due to the fact that SMS was easily decomposed at the lower temperatures accumulating large amounts of residues on the surface of TDS where the accumulation and condensation reactions acted to hinder or delay its decomposition (Chen et al., 2017a). To further discuss the co-combustion performance, the kinetic and thermodynamic analyses conducted are presented in the next sections.

3.5. Kinetic and thermodynamic characterizations of co-combustion performances

Apparent activation energy can be defined as the energy barriers for a chemical reaction to overcome. A single mechanism function is not suitable to describe the complex co-combustion processes. In order to obtain an accurate E_a, the two iso-conversional methods (FWO and KAS) were applied to the TG data at 10, 20 and 30 °C/min. Moisture became influential on the estimation of E_a at $\alpha = 0.1$, while mass

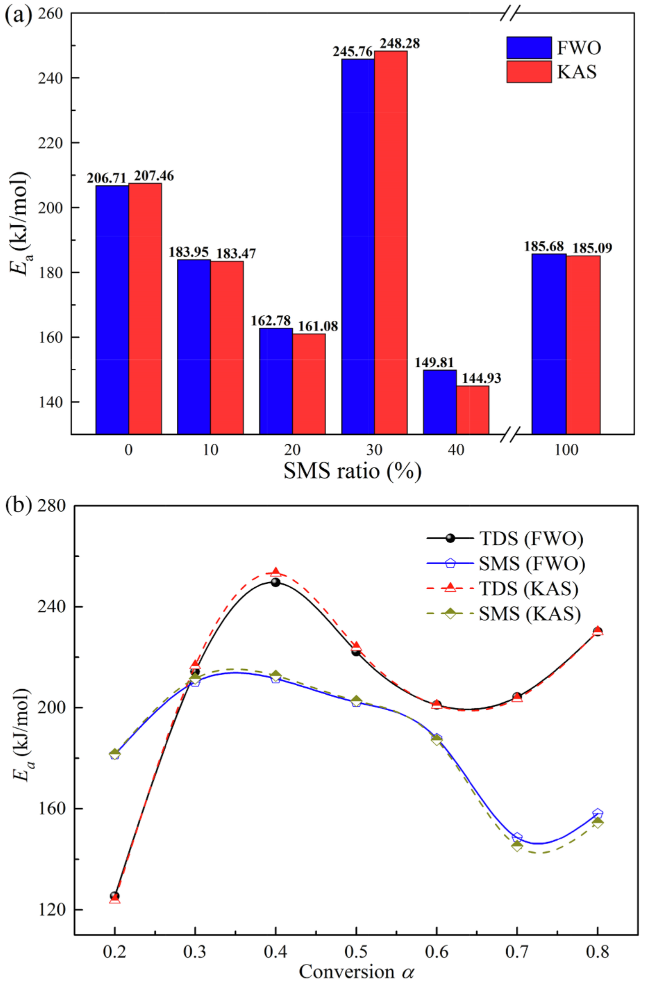

Fig. 3. Relationships between (a) apparent activation energy (E_a) and SMS fraction; and (b) E_a and conversion degree (α) based on the FWO and KAS methods.

transfer grew dominant in its estimation at $\alpha = 0.9$. Therefore, the E_a values were estimated in the range of 0.2–0.8. The E_a estimates by the two methods were very close regardless of the blend ratio, with the high R^2 values of over 0.93 (Fig. 3). The similar trends in E_a were exhibited with the increased α according to both FWO and KAS during the mono-combustions (Fig. 3b). α-dependent E_a values pointed to the involvement of the complicated reaction mechanisms in the co-combustion process (Barbanera et al., 2018).

The initially low E_a values of both TDS and SMS indicated their less energy requirement to start the chemical reaction (Fig. 3b). However, the lower E_a value of TDS than SMS at $\alpha = 0.2$ was due to the thermal stability. Such contents of TDS as dyes, slurries, dyeing auxiliaries, acids, bases, fibers, inorganic compounds, and labile chemical structures to be decomposed at high temperatures lowered its energy requirement (Peng et al., 2015). The increased E_a values between 0.2 and 0.4 may be due to the decompositions of carbohydrates and proteins in TDS and SMS, thus decreasing the C—O and C—H bonds. Since these chemical bonds have poor thermal stability, their reduction was reported to elevate the E_a values (Cao et al., 2016). In the ranges of 0.4–0.6 (277.0–352.4 °C) for TDS and 0.4–0.7 (302.8–377.4 °C) for SMS, the E_a values significantly declined. At these stages, the decomposition and release of volatiles may have formed a porous carbon structure which enhanced the diffusion of oxygen (Wang et al., 2016).

In the final reaction stage, the reason for the slight increase in E_a may be due to the decompositions of biochar, and the high boiling point inorganic compounds which required high energy (Cao et al., 2016; Hu et al., 2015). The lower average E_a estimate by FWO of SMS than TDS (Fig. 3a) appeared to stem from the thermal stability. The increased SMS did not necessarily decrease the average E_a value all the time. The mean E_a peaked (245.76 kJ/mol) with 30% SMS but was minimized (149.81 kJ/mol) with 40% SMS. In other words, the ease of the reaction with 40% SMS requiring less energy to promote the co-combustion process appeared to be the optimal choice of the blend ratio.

Table 3 shows the multiple comparisons of E_a, A, ΔH, ΔG, and ΔS as a function of the blend ratio and the conversion degree during the (co-)combustion process. The variation in the A values of the blends with the conversion rate by more than $10^9\,s^{-1}$ pointed to the complex compositions and combustion reactions (Maia and Morais, 2016). The A range was wider by several orders of magnitude for TDS than SMS. 40% SMS led to the narrowest range of A. The small difference between the E_a and ΔH values by < 7 kJ/mol (Table 3) showed that the reactions benefited the formation of the activated complex (Barbanera et al., 2018; Müsellim et al., 2018). The lower the ΔG value is, the more favorable the reaction is (Hui et al., 2015). The average ΔG value was lower for TDS (136.69 kJ/mol) than SMS (147.30 kJ/mol). Their mean values were lower than those of rice straw (164.59 kJ/mol) and rice bran (167.17 kJ/mol) which showed the less heat requirements of their combustion reactions (Maia and Morais, 2016). The negative ΔS and positive ΔG values also demonstrated that the combustions of these substances involved a non-spontaneous reaction.

3.6. *Reaction mechanisms of degradation of volatiles*

The reaction mechanisms of the individual biofuels, and 60TDS/40SMS were determined using the CR method for the releases of volatiles, and the char-burning stage. Based on the 17 common reaction models, the diffusion model, also known as the three-dimensional diffusion model (D3), was determined as the most suitable reaction mechanism with the highest R^2. All the R^2 values were above 96% when the D3 model was used though from the different heating rates and samples (Table 4). The good match between the calculated and experimental α (Fig. 4) indicated the reliability of the D3 model. The D3 model was shown to well describe the decomposition of lignocellulosic materials at the low temperature (Mallick et al., 2018). Fernandez-Lopez et al. (Fernandez-Lopez et al., 2016) found that the D3 model matched well with the devolatilization stage of manure and performed well in the reconstruction of the DTG curves. The D3 model was appropriate in the stages of devolatilization (180–350 °C) and char combustion (350–450 °C) for all the samples and heating rates (Table 4). The E_a estimates by the CR method were lower than those of the isoconversional methods, as discussed in Section 3.5. The E_a estimates from the model-free methods can be more reliable and should change as a function of α due to the complicated reactions of the entire combustion process. The E_a estimates by the CR method were the average values of the specific decomposition stages.

3.7. *Response surface methodology*

3.7.1. *Modeling*

The significance and adequacy of the best-fit quadratic models of ML and MLR according to BBD (Table 5) were evaluated using analysis of variance (ANOVA) (Joshi et al., 2018). The ANOVA results for the quadratic model of ML are shown in Table 6.

The best-fit quadratic regression model is provided below in terms of the coded factors:

$$\mathrm{ML}(\%) = 53.64 + 0.85\mathrm{A} + 7.26\mathrm{B} - 20.39\mathrm{C} - 0.27\mathrm{AB} - 0.004\mathrm{AC} + 4.95\mathrm{BC} + 1.35\mathrm{A}^2 + 0.60\mathrm{B}^2 + 18.98\mathrm{C}^2$$

The model predictors with a p-value < 0.05 were blend ratio, temperature, and quadratic temperature (Table 6). The lack-of-fit p value > 0.05 indicated that the model accurately fitted the ML data

Table 3
Multiple comparisons of one kinetic and four thermodynamic parameters as a function of blend ratio of TDS to SMS, and conversion degree (α) according to FWO and KAS methods..

Samples	α	FWO						KAS					
		E_a (kJ/mol)	R^2	A (s^{-1})	ΔH (kJ/mol)	ΔG (kJ/mol)	ΔS (J/mol)	E_a (kJ/mol)	R^2	A (s^{-1})	ΔH (kJ/mol)	ΔG (kJ/mol)	ΔS (J/mol)
TDS	0.2	125.39	0.9488	5.75E + 11	121.41	138.86	-32.11	123.78	0.9424	3.97E + 11	119.80	138.92	-35.18
	0.3	214.27	0.9747	3.42E + 20	209.95	136.44	135.26	216.61	0.9727	5.81E + 20	212.30	136.39	139.66
	0.4	249.62	0.9337	9.96E + 23	245.05	135.75	201.10	253.28	0.9292	2.27E + 24	248.70	135.68	207.95
	0.5	222.20	0.8771	2.06E + 21	217.36	136.28	149.19	223.90	0.8675	3.01E + 21	219.05	136.24	152.36
	0.6	201.12	0.9171	1.75E + 19	195.91	136.73	108.90	200.96	0.9090	1.69E + 19	195.75	136.73	108.59
	0.7	204.29	0.9527	3.59E + 19	198.76	136.66	114.26	203.62	0.9477	3.08E + 19	198.09	136.67	113.00
	0.8	230.11	0.9488	1.22E + 22	224.24	136.12	162.15	230.11	0.9437	1.22E + 22	224.25	136.12	162.15
90TDS/10SMS	0.2	120.93	0.9444	7.58E + 10	116.88	144.54	-49.11	118.95	0.9370	4.88E + 10	114.90	144.61	-52.77
	0.3	187.09	0.9629	1.61E + 17	182.69	142.49	71.39	187.86	0.9595	1.91E + 17	183.47	142.47	72.80
	0.4	209.41	0.9450	2.12E + 19	204.77	141.96	111.53	210.83	0.9403	2.89E + 19	206.20	141.93	114.13
	0.5	208.35	0.9511	1.68E + 19	203.49	141.99	109.22	209.26	0.9467	2.05E + 19	204.40	141.97	110.87
	0.6	181.40	0.9072	4.63E + 16	176.23	142.64	59.66	180.29	0.8973	3.63E + 16	175.12	142.67	57.64
	0.7	181.37	0.9325	4.59E + 16	175.85	142.64	58.98	179.54	0.9245	3.08E + 16	174.03	142.69	55.66
	0.8	199.14	0.9685	2.25E + 18	193.28	142.20	90.71	197.54	0.9647	1.58E + 18	191.68	142.24	87.81
80TDS/20SMS	0.2	150.27	0.9986	4.10E + 13	146.06	144.41	2.90	149.48	0.9984	3.44E + 13	145.26	144.44	1.45
	0.3	180.16	0.9978	2.81E + 16	175.66	143.56	56.68	180.33	0.9976	2.91E + 16	175.83	143.56	56.98
	0.4	181.60	0.9929	3.84E + 16	176.90	143.52	58.95	181.45	0.9922	3.72E + 16	176.75	143.53	58.67
	0.5	178.69	0.9876	2.04E + 16	173.80	143.60	53.34	178.00	0.9863	1.75E + 16	173.11	143.62	52.08
	0.6	155.93	0.9399	1.41E + 14	150.77	144.24	11.54	153.50	0.9321	8.31E + 13	148.34	144.31	7.12
	0.7	150.12	0.9542	3.96E + 13	144.62	144.42	0.36	146.68	0.9475	1.87E + 13	141.19	144.53	-5.90
	0.8	142.65	0.9682	7.70E + 12	136.82	144.66	-13.85	138.12	0.9629	2.85E + 12	132.29	144.81	-22.11
70TDS/30SMS	0.2	425.84	0.9997	4.09E + 39	421.50	139.02	500.41	439.10	0.9997	7.10E + 40	434.76	138.88	524.14
	0.3	278.26	1.0000	5.89E + 25	273.69	141.02	235.02	283.39	1.0000	1.79E + 26	278.82	140.93	244.27
	0.4	236.28	0.9960	6.52E + 21	231.54	141.79	159.00	238.90	0.9957	1.15E + 22	234.17	141.73	163.75
	0.5	234.18	0.9946	4.14E + 21	229.27	141.83	154.91	236.34	0.9942	6.62E + 21	231.43	141.78	158.81
	0.6	207.59	0.9583	1.27E + 19	202.41	142.39	106.32	207.83	0.9542	1.34E + 19	202.66	142.39	106.77
	0.7	180.98	0.9698	3.81E + 16	175.46	143.04	57.43	179.11	0.9661	2.53E + 16	173.59	143.09	54.03
	0.8	157.17	0.9783	2.07E + 14	151.29	143.70	13.45	153.32	0.9749	8.91E + 13	147.44	143.82	6.43
60TDS/40SMS	0.2	139.55	0.9997	3.99E + 12	135.18	144.65	-16.73	137.88	0.9996	2.76E + 12	144.71	133.51	-19.78
	0.3	153.93	0.9993	9.35E + 13	149.35	144.19	9.12	152.57	0.9992	6.94E + 13	144.23	147.99	6.64
	0.4	155.84	0.9994	1.42E + 14	151.11	144.13	12.33	154.27	0.9994	1.01E + 14	144.18	149.53	9.46
	0.5	165.22	0.9997	1.11E + 15	160.32	143.86	29.09	163.79	0.9997	8.10E + 14	143.90	158.89	26.50
	0.6	157.55	0.9966	2.06E + 14	152.40	144.08	14.70	138.30	0.9941	3.03E + 12	144.69	133.16	-20.39
	0.7	142.18	0.9949	7.10E + 12	136.68	144.56	-13.93	138.30	0.9941	3.03E + 12	144.69	132.80	-21.01
	0.8	134.43	0.9929	1.29E + 12	128.57	144.83	-28.73	129.38	0.9917	4.26E + 11	145.01	123.52	-37.97
SMS	0.2	181.48	0.9978	1.42E + 16	176.96	147.37	51.00	181.69	0.9976	1.49E + 16	177.16	147.37	51.37
	0.3	210.19	0.9990	6.35E + 18	205.52	146.66	101.46	211.58	0.9989	8.53E + 18	206.91	146.63	103.92
	0.4	211.50	0.9598	8.39E + 18	206.71	146.63	103.57	212.73	0.9562	1.09E + 19	207.94	146.61	105.74
	0.5	202.22	0.8196	1.17E + 18	197.31	146.85	86.99	202.73	0.8050	1.30E + 18	197.83	146.84	87.90
	0.6	187.80	0.9326	5.46E + 16	182.72	147.21	61.22	187.19	0.9254	4.80E + 16	182.11	147.22	60.15
	0.7	148.57	0.9844	1.27E + 13	143.16	148.34	−8.92	145.20	0.9818	6.17E + 12	139.80	148.45	−14.91
	0.8	158.00	0.9640	9.54E + 13	152.29	148.04	7.32	154.50	0.9585	4.51E + 13	148.78	148.15	1.09

(Lin et al., 2018). The model accounted for 91.9% of variation in ML. Based on the one-leave-out cross-validation, the predictive power (R^2_{pred}) of the model was also high (80.42%). Precision measures the signal-to-noise (S/N) ratio whose value being > 4 is considered desirable in which case this value for our model was 13.5. The coefficient of variation value of 8.39% demonstrated the good degree of precision and accuracy of the model (Joshi et al., 2018).

Our multiple non-linear regression results pointed to the quadratic

Table 4
(Co-)combustion kinetic models of two stages at three heating rates.

Sample	β (°C/min)	Devolatilization stage (D3)			Char combustion stage (D3)		
		Equation	R^2	E_a (kJ/mol)	Equation	R^2	E_a (kJ/mol)
TDS	10	$y = -4467.3x - 8.2700$	0.9961	37.14	$y = -3973.1x - 9.2367$	0.9962	33.03
	20	$y = -8806.5x - 0.2706$	0.9908	68.67	$y = -3652.2x - 9.8898$	0.9893	30.36
	30	$y = -8833.4x - 0.2609$	0.9915	69.55	$y = -3456.1x - 10.2080$	0.9885	28.73
60TDS/40SMS	10	$y = -6639.9x - 4.8466$	0.9656	55.20	$y = -3258.8x - 10.2690$	0.9992	27.09
	20	$y = -9283.6x - 0.1710$	0.9959	77.18	$y = -2993.1x - 10.8570$	0.9992	24.88
	30	$y = -9403.6x - 0.1627$	0.9963	78.18	$y = -2921.8x - 11.0410$	0.9989	24.29
SMS	10	$y = -9562.4x - 0.0100$	0.9975	79.50	$y = -3861.2x - 9.2146$	0.9800	32.10
	20	$y = -9811.5x + 0.0299$	0.9964	81.57	$y = -3363.3x - 10.1110$	0.9747	27.96
	30	y = −9836.7x – 0.1143	0.9271	81.78	y = −10224x – 0.0035	0.9990	85.00

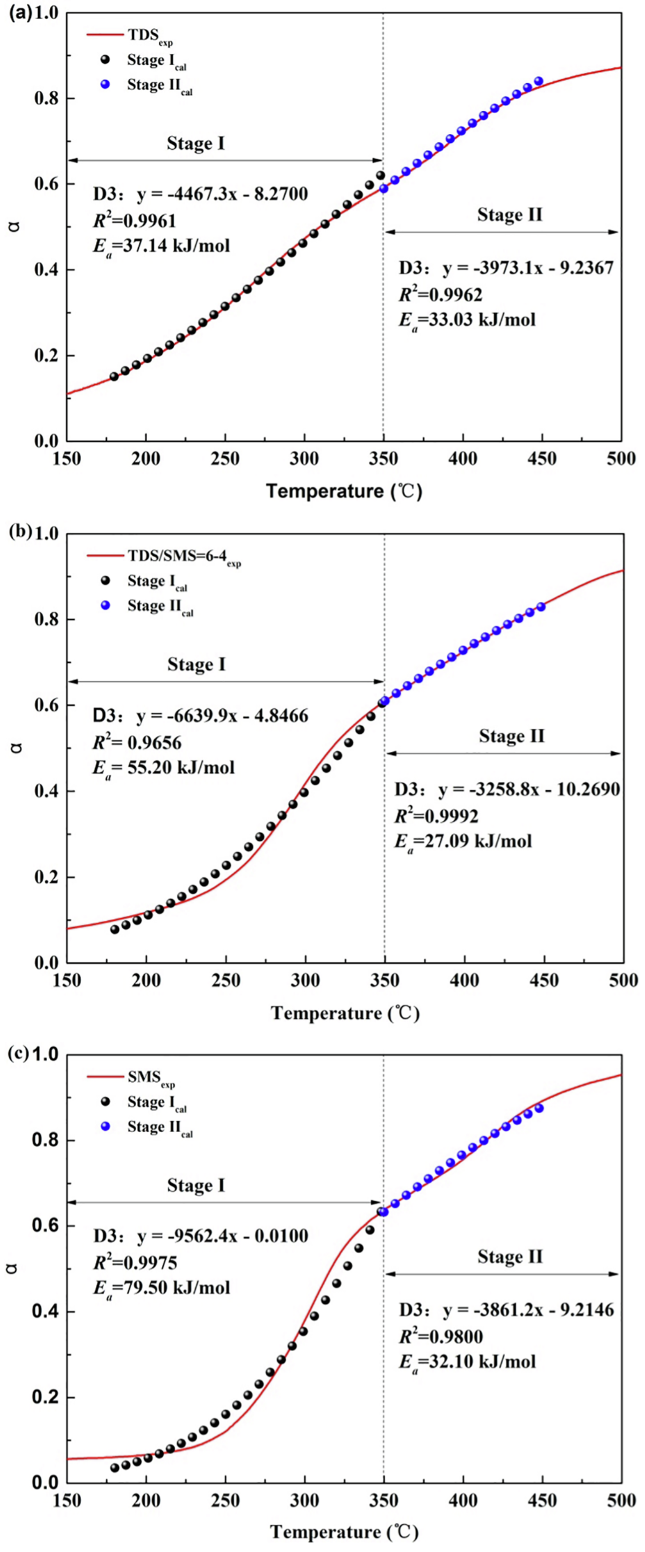

Fig. 4. Calculated versus experimental α using the D3 model at 10 °C/min.

Table 5
Box-Behnken design of three variables, and a comparison of experimental (exp) versus predicted (pred) responses of ML and MLR.

Variables	Symbol	Ranges and levels		
		Low	Mid	High
Heating rate (°C/min)	A	10	20	30
Blend ratio (%)	B	60	80	100
Temperature (°C)	C	200	600	1000

Std	Run	A	B	C	ML (%)		MLR (°C/min)	
					Exp	Pred	Exp	Pred
1	1	10	60	600	44.55	47.22	0.080	−0.264
17	2	20	80	600	56.32	53.64	0.184	0.219
7	3	10	80	1000	53.12	52.74	0.144	0.295
9	4	20	60	200	94.20	91.30	1.208	1.309
5	5	10	80	200	93.27	93.51	0.716	0.958
12	6	20	100	1000	62.13	65.03	0.716	0.615
13	7	20	80	600	56.32	53.64	0.184	0.219
10	8	20	100	200	93.64	95.92	1.582	1.388
11	9	20	60	1000	42.90	40.62	0.125	0.319
16	10	20	80	600	42.90	53.64	0.358	0.219
15	11	20	80	600	56.32	53.64	0.184	0.219
14	12	20	80	600	56.32	53.64	0.184	0.219
8	13	30	80	1000	54.66	54.42	0.954	0.711
4	14	30	100	600	66.09	63.42	0.213	0.556
2	15	30	60	600	46.93	49.44	0.419	0.468
3	16	10	100	600	64.78	62.26	0.070	0.021
6	17	30	80	200	94.83	95.23	1.962	1.812

Std: Standard run order; and Run: Random run order.

Table 6
Analysis of variance (ANOVA) results for mass loss (ML, %).

Source	SS	df	MS	*F*-value	*p*-value	VIF
Intercept	5405.14	9	600.57	21.18	0.0003	
A (heating rate)	5.74	1	5.74	0.20	0.6662	1
B (blend ratio)	421.28	1	421.28	14.86	0.0062	1
C (temperature)	3326.55	1	3326.55	117.34	< 0.0001	1
A * B	0.28	1	0.28	0.01	0.9230	1
A * C	0.00	1	0.00	0.00	0.9986	1
B * C	97.97	1	97.97	3.45	0.1054	1
A^2	7.73	1	7.73	0.27	0.6177	1
B^2	1.50	1	1.50	0.05	0.8246	1
C^2	1517.28	1	1517.28	53.50	0.0002	1
Residual	198.50	7	28.36			
Lack of fit	54.50	3	18.17	0.50	0.6996	
Pure error	144.00	4	36.00			
Total	5603.64	16				
SD	5.32		R^2_{adj} (%)	91.90		
Mean	63.49		R^2_{pred} (%)	80.42		
CV (%)	8.39		Precision	13.5		
PRESS	1096.98					

df: degrees of freedom; SS: sum of squares; MS: mean squares; VIF: variation inflation factor; *F*-value: Fisher test value; *p*-value: significance level; SD: standard deviation; CV: coefficient of variation; PRESS: predicted residual sum of squares.

model as the best-fit one with the following coded factors:

$$\text{MLR (\%/min)} = 0.22 + 0.32\text{A} + 0.094\text{B} - 0.44\text{C} - 0.49\text{AB} - 0.11\text{AC} + 0.054\text{BC} + 0.006\text{A}^2 - 0.030\text{B}^2 + 0.72\text{C}^2$$

where A, B and C refer to heating rate (°C/min), blend ratio (%), and temperature (°C), respectively. The model elucidated 76.95% of variation in MLR, with an R^2_{pred} of 54.6%. The optimal operational values were estimated at 15.90 °C/min for heating rate, 60/40% for the TDS/SMS ratio, and 867.0 °C for ML and 30 °C/min, 60/40% and 1000 °C for MLR. These conditions were consistent with the conclusions drawn in Sections 3.5. Under the optimal conditions, the maximized ML and MLR values were determined as 38.29% and 47.43%/min, respectively.

3.7.2. *Effects of operational parameters*

The significant predictors of ML and MLR determined in this study were consistent with the results by (Liu et al., 2017). Their effects on the response variables are depicted in Fig. 5. According to the effects of the blend ratio and temperature on ML (Fig. 5a), the ML value was maximized with the increased temperature, and the low TDS fraction at

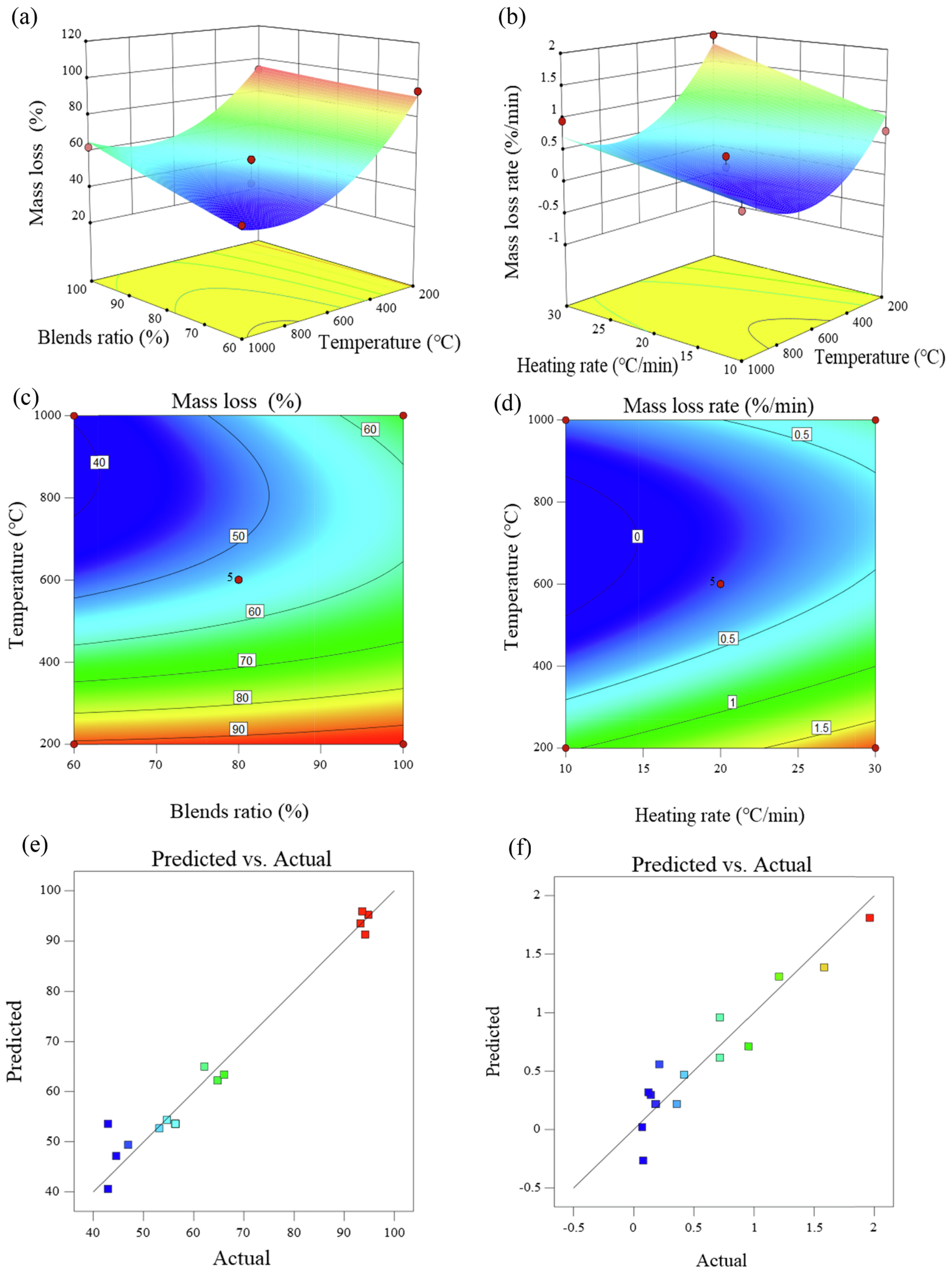

Fig. 5. (a and b) 3D surface, (c and d) contour and (e and f) predicted versus actual value plots for effects of significant variables on ML and MLR.

20 °C/min. No significant difference was found at the low temperature despite the addition of more SMS. This suggested that the interaction between the blend ratio and temperature existed at the high temperatures.

Fig. 5b shows the increased MLR with the increased heating rate due to its more energy supply as well as the higher MLR at the low temperatures due to the combustion of volatiles matters. Fig. 5c and d suggest that the SMS fraction and temperature should be over 42% and 750 °C, respectively. MLR was close to zero in the range of 500–850 °C at below 15 °C/min (Fig. 5d). This was consistent with the DTG curve in Section 3.1. Fig. 5e and f show that the quadratic model was more suitable to describe ML than MLR as was also verified by their R^2 values of 96.46 and 89.92%, respectively.

3.8. TG-MS analysis

The emissions of pollutant gases from TDS and 40% SMS were analyzed using TG-MS data. Fig. 6 shows the intensity changes in NH_3

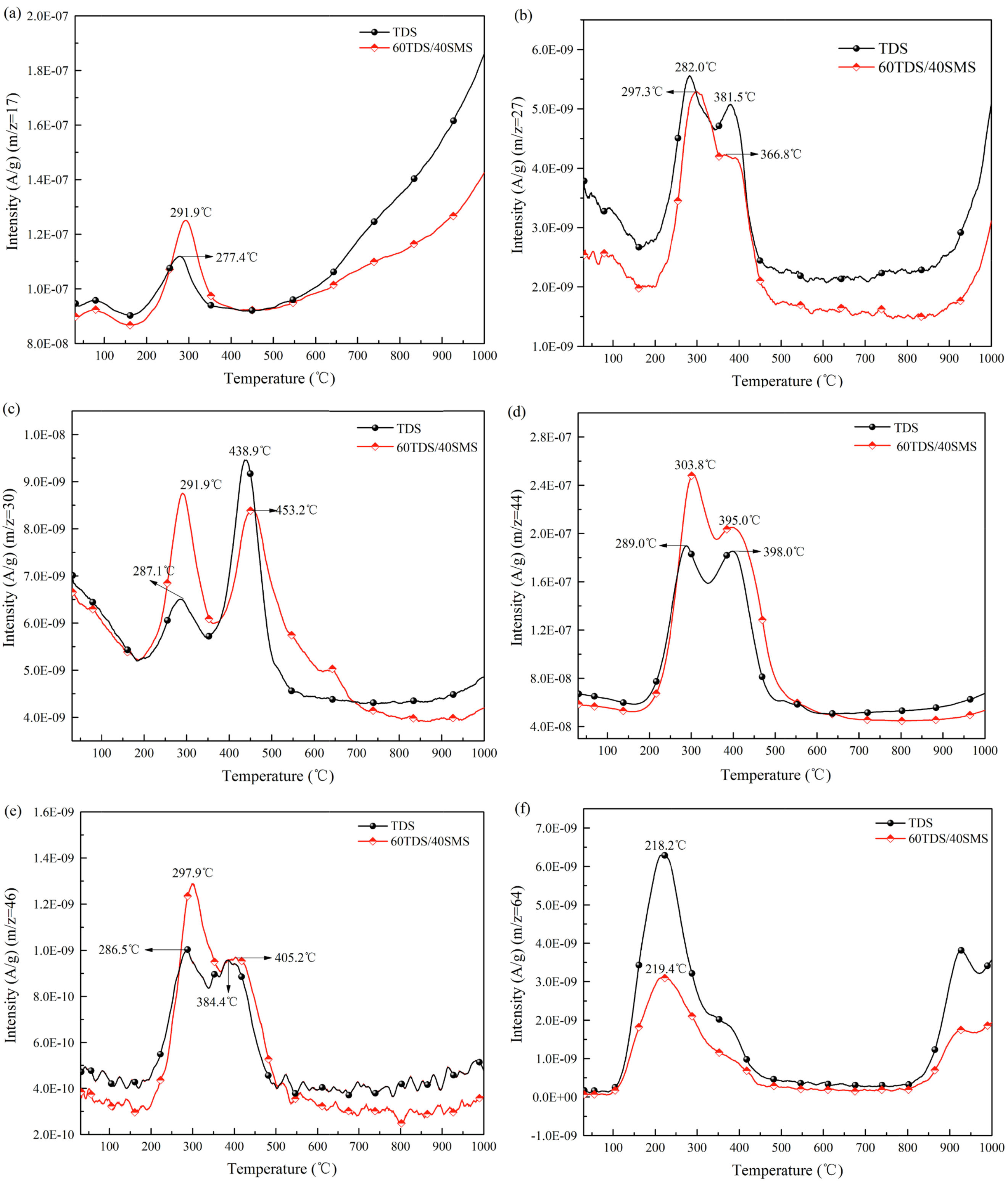

Fig. 6. The ion intensity of gaseous products according to TG-MS analysis: (a) $m/z = 17$; (b) $m/z = 27$; (c) $m/z = 30$; (d) $m/z = 44$; (e) $m/z = 46$; and (f) $m/z = 64$.

($m/z = 17$), HCN ($m/z = 27$), NO ($m/z = 30$), CO_2 ($m/z = 44$), NO_2 ($m/z = 46$), and SO_2 ($m/z = 64$). Their emission peaks were all located in the range of 200–500 °C. HCN and NH_3 are the intermediate species to form NO_x during the combustion of the fuel N, and their emissions were significant to evaluate the transformation of N species (Shah et al., 2018). Fig. 6a and b showed that with the addition of 40% SMS to TDS, the emission peak of NH_3 and HCN moved toward a higher temperature which indicated the higher binding energy and stronger stability of N-containing compounds in SMS (Gong et al., 2019). Li and Tan (2000) stated that HCN was mainly generated from the decomposition of N-containing structures with low thermal stability, while thermally stable N-containing structures controlled the generation of NH_3. However, our results showed the higher emission intensity and easier emission peak of NH_3 than HCN during the devolatilization stage. This finding was consistent with other results that more NH_3 was released directly prior to HCN during the devolatilizing stage of biomass combustion, thus leading to the partial transformation of NH_3 into HCN according to the following reaction: $NH_3 + CH \rightarrow HCN$ (Fig. 6a and b) (Moroń and Rybak, 2015; Shah et al., 2018). The addition of 40% SMS accelerated the NH_3 emission and lowered the HCN emission. The higher H content of SMS than TDS seemed to provide more H radicals to promote the NH_3 emission from the devolatization stage (Li and Tan, 2000). The N contents of fuel and remaining char were reported to result in more NH_3 and HCN releases at above 800 °C (Aho et al., 1993; Zhou et al., 2018).

There were the two peaks of NO and NO_2 emissions for TDS, while the first peak temperature was slightly lower for NO (284.6 °C) than NO_2 (288.4 °C) (Fig. 6c and e). This trends also existed with 40% SMS. NO is known to be the predominant N-containing gaseous species when the oxidation of NO to NO_2 in the air atmosphere occurs easily in a high atmospheric pressure and at a low temperature (Wang et al., 2018a). The NO formation involved a complex process mainly depending on the fuel type and the combustion conditions, while the main source of NO was the oxidation of fuel-bound N at below 1500 °C in a combustion system (Yanik et al., 2018). The strengthened first emission peaks of NO and NO_2, and their weakened second peaks with 40% SMS indicated more NO_x releases from the stages of volatiles combustion and inorganic N decomposition at below 300 °C (Tian et al., 2013). The maximum emission peak of SMS at 540 °C reported by our previous study (Huang et al., 2018) did not appear in the present study suggesting an interaction to accelerate the char combustion, and the release of more NO_x emissions. Fig. 6d shows the CO_2 emission with the risen temperature whose two peaks representing the combustions of volatiles matters and fixed carbon, respectively. 40% SMS enhanced the CO_2 emission, in particular, for the first peak due to its higher C content than TDS (Table 1).

Fig. 6f shows that 40% SMS decreased the intensity of SO_2 emission due to its low S content. The first peak of SO_2 at 220 °C for TDS and 40% SMS indicated that most S existed in the form of organic S that was released upon the combustion of volatiles matters. The emission peak of SO_2 at 320 °C according to our previous study (Huang et al., 2018) suggested that the S content of TDS had lower thermal stability, as was consistent with the lower ignition activation energy of TDS than SMS.

The increased SO_2 emission at above 800 °C showed that the inorganic S decomposed at the high temperature. The intensity of TDS with 40% SMS was lower than that of the pure TDS due to the lower inorganic S. The additional peak of SO_2 at about 900 °C appeared to relate to the decomposition of $CaSO_4$ or other inorganic S-containing structures such as Na_2SO_4. Since TDS contained a large amount of Na and Si, the following reaction at the high temperature may occur to promote the generation of SO_2: $Na_2SO_4 + 6SiO_2 + Al_2O_3 \rightarrow 2NaAlSi_3O_8 + SO_2 + 0.5O_2$ (Qi et al., 2018). CaO as a common disinfectant found in SMS can effectively absorb SO_2 to form $CaSO_4$. $CaSO_4$ decomposes to CaO and SO_2 between 800 and 1000 °C according to the following equation: $CaSO_4 \rightarrow CaO + SO_2$ (Wang et al., 2008; Yanik et al., 2018). According to Table 1, the high P content of SMS may promote the degradation of $CaSO_4$ following the reaction: $3CaSO_4 + P_2O_5 \rightarrow Ca_3(PO_4)_2 + 3SO_2 + 1.5O_2$ (Qi et al., 2018). Hence, with Ca and P present in the combustion system at the high temperature, it is easier to generate more SO_2. At low-to-moderate temperatures, the organic S was thermally decomposed during the devolatilization stage, while the inorganic S was shown to decompose through interaction with the matrix at above 900 °C (Ren et al., 2017). The SO_2 emission peak at the high temperature was consistent with the (D)TG curves that a small amount of inorganic matters was degraded at above 900 °C.

4. Conclusions

The addition of SMS to TDS significantly increased $-R_P$, D_i, D_b, and *CCI*, indicative of the improved co-combustion performance. The thermal degradation lowered T_i by 59.6 °C for TDS relative to SMS. The interaction occurred mainly between 350 and 600 °C during the combustion stage of fixed carbon, and that the minerals may have catalyzed the combustion process. The minimum mean E_a obtained with 40% SMS pointed to it as the optimal blend ratio. The addition of 40% SMS to TDS decreased the HCN and SO_2 emissions but released more NO and NO_2 emissions at the lower temperature.

Acknowledgments

This research was financially supported by the National Natural Science Foundation of China (No. 51608129), the Scientific and Technological Planning Project of Guangzhou, China (Nos. 201704030109 and 2016201604030058), and the Science and Technology Planning Project of Guangdong Province, China (Nos. 2019B020208017, 2018A050506046, 2015B020235013, 2017A050501036 and 2016A050502059).

Appendix A. Supplementary material

Supplementary data to this article can be found online at https://doi.org/10.1016/j.biortech.2019.02.011.

References

Aho, M.J., Hämäläinen, J.P., Tummavuori, J.L., 1993. Importance of solid fuel properties to nitrogen oxide formation through HCN and NH_3 in small particle combustion. Combust. Flame 95, 22–30.

Barbanera, M., Cotana, F., Di Matteo, U., 2018. Co-combustion performance and kinetic study of solid digestate with gasification biochar. Renew. Energy 121, 597–605.

Buyukada, M., 2017b. Uncertainty estimation by Bayesian approach in thermochemical conversion of walnut hull and lignite coal blends. Bioresour. Technol. 232, 87–92.

Buyukada, M., 2017a. Probabilistic uncertainty analysis based on Monte Carlo simulations of co-combustion of hazelnut hull and coal blends: Data-driven modeling and response surface optimization. Bioresour. Technol. 225, 106–112.

Cai, J., Xu, D., Dong, Z., Yu, X., Yang, Y., Banks, S.W., Bridgwater, A.V., 2018. Processing thermogravimetric analysis data for isoconversional kinetic analysis of lignocellulosic biomass pyrolysis: case study of corn stalk. Renew. Sust. Energy Rev. 82, 2705–2715.

Cao, L., Yuan, X., Jiang, L., Li, C., Xiao, Z., Huang, Z., Chen, X., Zeng, G., Li, H., 2016. Thermogravimetric characteristics and kinetics analysis of oil cake and torrefied biomass blends. Fuel 175, 129–136.

Chen, C., Qin, S., Chen, F., Lu, Z., Cheng, Z., 2017a. Co-combustion characteristics study of bagasse, coal and their blends by thermogravimetric analysis. J. Energy Inst. https://doi.org/10.1016/j.joei.2017.12.008.

Chen, J., Wang, Y., Lang, X., Ren, X., Fan, S., 2017b. Comparative evaluation of thermal oxidative decomposition for oil-plant residues via thermogravimetric analysis: thermal conversion characteristics, kinetics, and thermodynamics. Bioresour. Technol. 243, 37–46.

Deng, S., Wang, X., Tan, H., Mikulčić, H., Yang, F., Li, Z., Duić, N., 2016. Thermogravimetric study on the Co-combustion characteristics of oily sludge with plant biomass. Thermochim. Acta 633, 69–76.

Dong, H., Jiang, X., Lv, G., Wang, F., Huang, Q., Chi, Y., Yan, J., Yuan, W., Chen, X., Lu, W., 2017. Co-combustion of tannery sludge in a bench-scale fluidized-bed combustor: gaseous emissions and Cr distribution and speciation. Energy Fuels 31, 11069–11077.

Fernandez-Lopez, M., Pedrosa-Castro, G.J., Valverde, J.L., Sanchez-Silva, L., 2016. Kinetic analysis of manure pyrolysis and combustion processes. Waste Manage. 58, 230–240.

Gil, M.V., Casal, D., Pevida, C., Pis, J.J., Rubiera, F., 2010. Thermal behaviour and kinetics of coal/biomass blends during co-combustion. Bioresour. Technol. 101, 5601–5608.

Gong, Z., Wang, Z., Wang, Z., Fang, P., Meng, F., 2019. Study on the migration characteristics of nitrogen and sulfur during co-combustion of oil sludge char and microalgae residue. Fuel 238, 1–9.

Guo, F., Zhong, Z., 2018b. Optimization of the co-combustion of coal and composite biomass pellets. J. Clean. Prod. 185, 399–407.

Guo, F., Zhong, Z., 2018a. Co-combustion of anthracite coal and wood pellets: thermodynamic analysis, combustion efficiency, pollutant emissions and ash slagging. Environ. Pollut. 239, 21–29.

Hu, S., Ma, X., Lin, Y., Yu, Z., Fang, S., 2015. Thermogravimetric analysis of the co-combustion of paper mill sludge and municipal solid waste. Energy Convers. Manage. 99, 112–118.

Huang, J., Liu, J., Chen, J., Xie, W., Kuo, J., Lu, X., Chang, K., Wen, S., Sun, G., Cai, H., Buyukada, M., Evrendilek, F., 2018. Combustion behaviors of spent mushroom substrate using TG-MS and TG-FTIR: thermal conversion, kinetic, thermodynamic and emission analyses. Bioresour. Technol. 266, 389–397.

Hui, L., Niu, S.L., Lu, C.M., Cheng, S.Q., 2015. Comparative evaluation of thermal degradation for biodiesels derived from various feedstocks through transesterification. Energy Convers. Manage. 98, 81–88.

Jiang, L., Zhang, D., Li, M., He, J.-J., Gao, Z.-H., Zhou, Y., Sun, J.-H., 2018. Pyrolytic behavior of waste extruded polystyrene and rigid polyurethane by multi kinetics methods and Py-GC/MS. Fuel 222, 11–20.

Joshi, S.M., Gogate, P.R., Suresh Kumar, S., 2018. Intensification of esterification of karanja oil for production of biodiesel using ultrasound assisted approach with optimization using response surface methodology. Chem. Eng. Process. 124, 186–198.

Latchubugata, C.S., Kondapaneni, R.V., Patluri, K.K., Virendra, U., Vedantam, S., 2018. Kinetics and optimization studies using response surface methodology in biodiesel production using heterogeneous catalyst. Chem. Eng. Res. Des. 135, 129–139.

Li, X.G., Lv, Y., Ma, B.G., Jian, S.W., Tan, H.B., 2011. Thermogravimetric investigation on co-combustion characteristics of tobacco residue and high-ash anthracite coal. Bioresour. Technol. 102, 9783–9787.

Li, C.-Z., Tan, L.L., 2000. Formation of NOx and SOx precursors during the pyrolysis of coal and biomass. Part III. Further discussion on the formation of HCN and NH_3 during pyrolysis. Fuel 79, 1899–1906.

Lin, J., Su, B., Sun, M., Chen, B., Chen, Z., 2018. Biosynthesized iron oxide nanoparticles used for optimized removal of cadmium with response surface methodology. Sci. Total. Environ. 627, 314–321.

Liu, J., Huang, L., Buyukada, M., Evrendilek, F., 2017. Response surface optimization, modeling and uncertainty analysis of mass loss response of co-combustion of sewage sludge and water hyacinth. Appl. Therm. Eng. 125, 328–335.

Liu, Z., Zhang, Y., Zhong, L., Orndroff, W., Zhao, H., Cao, Y., Zhang, K., Pan, W.-P., 2013. Synergistic effects of mineral matter on the combustion of coal blended with biomass. J. Therm. Anal. Calorim. 113, 489–496.

Liu, Z., Zhang, T., Zhang, J., Xiang, H., Yang, X., Hu, W., Liang, F., Mi, B., 2018b. Ash fusion characteristics of bamboo, wood and coal. Energy 161, 517–522.

Liu, J., Zhuo, Z., Xie, W., Kuo, J., Lu, X., Buyukada, M., Evrendilek, F., 2018a. Interaction effects of chlorine and phosphorus on thermochemical behaviors of heavy metals during incineration of sulfur-rich textile dyeing sludge. Chem. Eng. J. 351, 897–911.

Ma, Q., Han, L., Huang, G., 2017. Potential of water-washing of rape straw on thermal properties and interactions during co-combustion with bituminous coal. Bioresour. Technol. 234, 53–60.

Maia, A.A.D., Morais, L.C.D., 2016. Kinetic parameters of red pepper waste as biomass to solid biofuel. Bioresour. Technol. 204, 157–163.

Mallick, D., Poddar, M.K., Mahanta, P., Moholkar, V.S., 2018. Discernment of synergism in pyrolysis of biomass blends using thermogravimetric analysis. Bioresour. Technol. 261, 294–305.

Moroń, W., Rybak, W., 2015. NOx and SO_2 emissions of coals, biomass and their blends under different oxy-fuel atmospheres. Atmos. Environ. 116, 65–71.

Müsellim, E., Tahir, M.H., Ahmad, M.S., Ceylan, S., 2018. Thermokinetic and TG/DSC-FTIR study of pea waste biomass pyrolysis. Appl. Therm. Eng. 137, 54–61.

Peng, X., Ma, X., Xu, Z., 2015. Thermogravimetric analysis of co-combustion between microalgae and textile dyeing sludge. Bioresour. Technol. 180, 288–295.

Qi, X., Song, G., Song, W., Yang, S., Lu, Q., 2018. Combustion performance and slagging characteristics during co-combustion of Zhundong coal and sludge. J. Energy. Inst. 91, 397–410.

Ren, X., Sun, R., Meng, X., Vorobiev, N., Schiemann, M., Levendis, Y.A., 2017. Carbon, sulfur and nitrogen oxide emissions from combustion of pulverized raw and torrefied biomass. Fuel 188, 310–323.

Shah, I.A., Gou, X., Zhang, Q., Wu, J., Wang, E., Liu, Y., 2018. Experimental study on NOx emission characteristics of oxy-biomass combustion. J. Clean. Prod. 199, 400–410.

Shi, W., Kong, L.-X., Bai, J., Xu, J., Li, W., Bai, Z., Li, W., 2018. Effect of CaO/Fe_2O_3 on fusion behaviors of coal ash at high temperatures. Fuel Process. Technol. 181, 18–24.

Tian, Y., Zhang, J., Zuo, W., Chen, L., Cui, Y., Tan, T., 2013. Nitrogen conversion in relation to NH_3 and HCN during microwave pyrolysis of sewage sludge. Environ. Sci. Technol. 47, 3498–3505.

Wang, Z., Hong, C., Xing, Y., Li, Y., Feng, L., Jia, M., 2018b. Combustion behaviors and kinetics of sewage sludge blended with pulverized coal: with and without catalysts. Waste Manage. 74, 288–296.

Wang, X., Jin, Y., Wang, Z., Mahar, R.B., Nie, Y., 2008. A research on sintering characteristics and mechanisms of dried sewage sludge. J. Hazard. Mater. 160, 489–494.

Wang, C.A., Wang, P., Du, Y., Che, D., 2018a. Experimental study on effects of combustion atmosphere and coal char on NO_2 reduction under oxy-fuel condition. J. Energy Inst. https://doi.org/10.1016/j.joei.2018.07.004.

Wang, G., Zhang, J., Shao, J., Liu, Z., Zhang, G., Xu, T., Guo, J., Wang, H., Xu, R., Lin, H., 2016. Thermal behavior and kinetic analysis of co-combustion of waste biomass/low rank coal blends. Energy Convers. Manage. 124, 414–426.

Wang, Q., Zhao, W., Liu, H., Jia, C., Li, S., 2011. Interactions and kinetic analysis of oil shale semi-coke with cornstalk during co-combustion. Appl. Energy 88, 2080–2087.

Xie, C., Liu, J., Zhang, X., Xie, W., Sun, J., Chang, K., Kuo, J., Xie, W., Liu, C., Sun, S., Buyukada, M., Evrendilek, F., 2018b. Co-combustion thermal conversion characteristics of textile dyeing sludge and pomelo peel using TGA and artificial neural networks. Appl. Energy 212, 786–795.

Xie, C., Liu, J., Xie, W., Kuo, J., Lu, X., Zhang, X., He, Y., Sun, J., Chang, K., Xie, W., Liu, C., Sun, S., Buyukada, M., Evrendilek, F., 2018a. Quantifying thermal decomposition regimes of textile dyeing sludge, pomelo peel, and their blends. Renew. Energy 122, 55–64.

Yanik, J., Duman, G., Karlström, O., Brink, A., 2018. NO and SO_2 emissions from combustion of raw and torrefied biomasses and their blends with lignite. J. Environ. Manage. 227, 155–161.

Zhou, H., Li, Y., Li, N., Qiu, R., Cen, K., 2018. Conversions of fuel-N to NO and N_2O during devolatilization and char combustion stages of a single coal particle under oxy-fuel fluidized bed conditions. J. Energy Inst. https://doi.org/10.1016/j.joei.2018.01.001.